

In situ monitoring of X-ray strain pole figures of a biaxially deformed ultra-thin film on a flexible substrate

G. Geandier,^a D. Faurie,^{b*} P.-O. Renault,^c D. Thiaudière^d and E. Le Bourhis^c

^aInstitut Jean Lamour, CNRS UMR7198, Université de Lorraine, Nancy Cedex, France, ^bLSPM-CNRS, UPR3407, Université Paris13, Villetaneuse, France, ^cInstitut Pprime UPR3346, CNRS – Université de Poitiers, Futuroscope, France, and ^dSOLEIL Synchrotron, Saint-Aubin, Gif-Sur-Yvette, France. Correspondence e-mail: faurie@univ-paris13.fr

Received 27 June 2013
Accepted 8 November 2013

X-ray strain pole figures (SPFs) have been captured *in situ* during biaxial deformation of a gold ultra-thin film (thickness = 40 nm) deposited on a polymer substrate. An area detector was used to extract one line in the reciprocal space while the strained sample was rotated azimuthally step by step to produce the SPF. Such SPFs have been obtained for a textured anisotropic ultra-thin film under controlled non-equibiaxial loading using the SOLEIL synchrotron DIFFABS tensile device. The experimental setup allows the pole figure measurements of {111} and {200} reflections to be performed simultaneously. Interestingly, those two crystallographic directions are related to the two-extreme elastic mechanical behaviour. The full directional lattice strain dependence (SPF) is obtained within 15 min and can be monitored step by step upon loading. This procedure gives an insight into ultra-thin film mechanical response under complex biaxial loading.

© 2014 International Union of Crystallography

1. Introduction

Understanding the mechanical behaviour of nanostructured thin films in relation to their microstructure is of utmost importance when technological applications are targeted (Leyland & Matthews, 2000; Mayrhofer *et al.*, 2006; Meyers *et al.*, 2006; Fu & Wagner, 2007). Actually, for nanometre length scales, mechanical properties are significantly altered compared with coarse-grained polycrystalline materials (Gleiter, 2000; Van Swygenhoven & Weertman, 2006; Meyers *et al.*, 2006; Kiener *et al.*, 2008). The processes responsible for these changes may be caused by an increase in grain-surface and grain-boundary volumes, which become dominant over the bulk at the nanoscale. In an ultra-thin film (<50 nm), changes are further caused by boundary conditions at the free surface and interface with the substrate, which become non-negligible (Arzt, 1998; Dingreville *et al.*, 2005). On the other hand, the mechanical behaviour of metallic stiff thin films attached to a flexible substrate poses a significant challenge in the development of integrated structures such as flexible and stretchable electronics (Lacour *et al.*, 2005; Rogers *et al.*, 2010; Koo *et al.*, 2012).

In situ synchrotron X-ray diffraction (XRD) is well known as a trustworthy and powerful tool to determine the mechanical properties of small-sized crystalline materials such as thin films (Faurie *et al.*, 2009; Djaziri *et al.*, 2013; Van Swygenhoven & Van Petegem, 2013). It is a phase-selective and nondestructive technique that allows for studying both the mechanical behaviour and the microstructure of diffracting phases (Martinschitz *et al.*, 2009; Richard *et al.*, 2013). As

crystalline materials are heterogeneous from the mechanical point of view, X-ray or neutron strain measurements have to be carried out for several diffraction vector directions and for different *hkl* reflections (Clausen *et al.*, 1999; Keckes *et al.*, 2012). In order to obtain the necessary results for orientation studies and to accomplish the mechanical behaviour analysis in a reasonably cost-effective time frame, the combination of area (or two-dimensional) detectors and X-ray synchrotron radiation is a suitable solution (Geandier *et al.*, 2008; Aydiner *et al.*, 2009). High throughput of materials analysis without sacrificing data quality is possible. Area detectors provide simultaneous collection of diffraction data from several lattice planes (Faurie *et al.*, 2011), thus allowing a more complete assessment and understanding of the mechanical behaviour of crystalline thin films (Aydiner *et al.*, 2009). Moreover, they allow the determination of the full strain pole figure (SPF) of a polycrystalline material (Bernier & Miller, 2006; Schuren *et al.*, 2012). This kind of representation of the strain field should be very helpful for studying heterogeneous mechanical behaviour and especially for estimating the strain partitioning. Unfortunately, experimental SPFs are rare in the literature for bulk materials (see, for example, Miller *et al.*, 2005; Bernier & Miller, 2006; Schuren *et al.*, 2012). To the best of our knowledge, such representations are not available for thin films, in particular under applied load.

The loading conditions of materials in use are often non-equibiaxial, *i.e.* anisotropic in-plane deformations. Moreover, the material itself may be anisotropic either locally (elastically and/or plastically) or macroscopically (if textured; Faurie *et al.*,

2006). Hence, to better understand the mechanical behaviour of thin films, it is necessary to acquire measurement data on several reflections with independent Miller indices and several directions in the reciprocal space for a given reflection, *i.e.* a combination of multidirection and multireflection, that is to extract an SPF.

In this article, we propose a method based on area detection, to acquire SPFs in a reasonable time (a few minutes). This method is applied to a gold ultra-thin film (40 nm) submitted to a complex biaxial loading path by using a recently developed synchrotron biaxial tensile tester (Geandier *et al.*, 2010). The {111} and {200} SPFs are measured for each loading step, comprising equibiaxial and non-equibiaxial stress states.

2. Experimental details and methodology

2.1. Ultra-thin film fabrication

An Au thin film was deposited on a 127.5 μm -thick polyimide (Kapton) cruciform substrate, 20 mm in width and 5 mm toe weld. The substrate was cleaned with ethanol before deposition. The film was deposited by continuous ion-beam sputtering. The base pressure in the growth chamber was 7×10^{-5} Pa, while the working pressure during film growth was approximately 10^{-2} Pa. Gold deposition was carried out at room temperature with an Ar^+ -ion-gun sputtering beam at 1.2 keV. The total thickness was measured to be 40 nm by X-ray reflectometry. Under these conditions, a {111} fiber texture with a dispersion of about 20° (FWHM) is obtained.

2.2. Controlled biaxial testing of supported ultra-thin film

We employed the DIFFABS-SOLEIL biaxial tensile device working in the synchrotron environment for *in situ* diffraction characterization of the thin polycrystalline film's mechanical

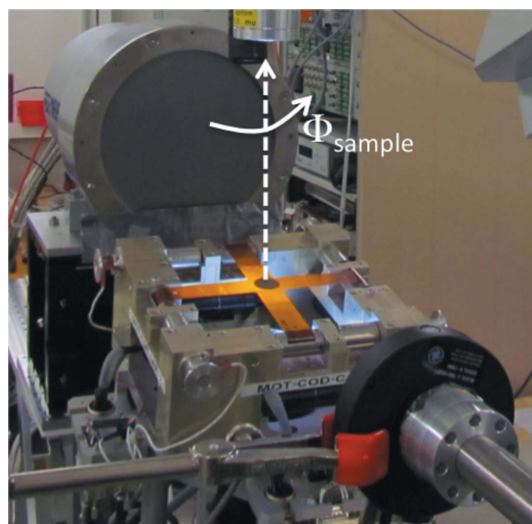


Figure 1 Setup used to test the cruciform substrate coated by the studied film and to record the diffractogram patterns. *In situ* tensile tests of thin films under biaxial loading were carried out on the DIFFABS beamline at SOLEIL. Φ_{sample} is the machine azimuthal angle.

response (Geandier *et al.*, 2010). The setup within the DIFFABS experimental station at SOLEIL (Saint-Aubin, France) is shown in Fig. 1. The biaxial loading device is shown mounted on the goniometer and allows for X-ray diffraction in the reflection mode at glancing angles (limited shadowing edges). Two pairs of motors and force sensors are fixed to the device frame. The four motors can be actuated separately in order to keep the studied area at a fixed position in the goniometer. The cruciform substrates were coated at their centre only and gripped by a cam rotating in a cylindrical fixation. The X-ray diffracted signal was recorded by a Mar SX-165 CCD detector placed at 160 mm from the sample (Fig. 2). The samples were mounted with an incident angle ω of 6° with an X-ray beam energy of 8.8 keV ($\lambda = 0.14089$ nm). The used X-ray beam cross section at the goniometer centre was 1×0.3 mm. In addition, the in-plane macroscopic strains of the polyimide substrate (opposite surface) were measured by digital image correlation (DIC; Hild *et al.*, 2009; Djaziri *et al.*, 2011).

2.3. Measurement method

Both {111} and {200} plane families could be monitored thanks to the two-dimensional detector (Fig. 2). Therefore, a single acquisition provides strain measurements in several orientations of a pole figure, as shown by Faurie *et al.* (2013) and recalled briefly below.

Changes in interplanar spacing d_{hkl} can be used with the Bragg law to determine the elastic strain $\varepsilon_{\varphi\psi}$ through the knowledge of the incident wavelength λ and the change in the Bragg scattering angle 2θ :

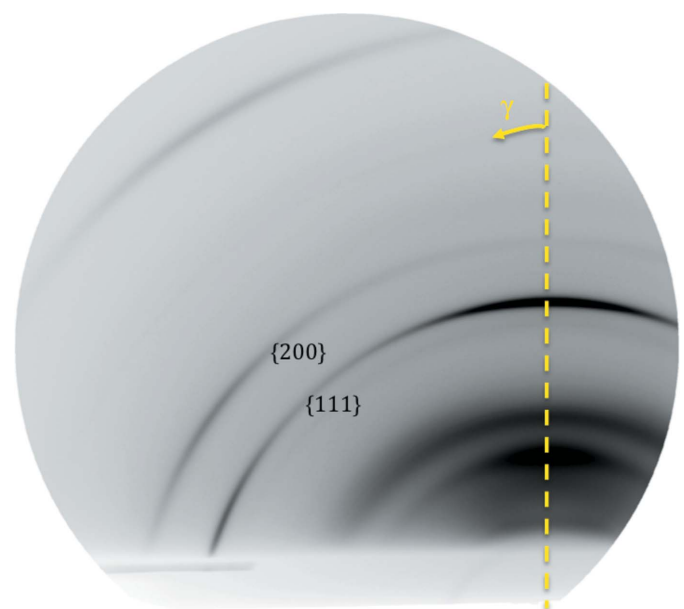


Figure 2 Whole two-dimensional diffraction pattern of the gold thin film under biaxial loading, obtained at the DIFFABS beamline in reflection mode. γ is the angle used to describe a Debye-Scherrer ring and to define the γ path. We can see clearly the {111} and {200} rings. The central diffuse signal is the X-ray signature of the supporting polyimide substrate.

$$\varepsilon_{\varphi\psi} = \ln(d_{hkl}/d_0) = \ln(\sin \theta_0 / \sin \theta), \quad (1)$$

where d_0 and θ_0 correspond to the reference state.

Employing an X-ray area detector, in-grain strain measurements can be monitored for several directions of the diffraction vector $\mathbf{k} = \mathbf{k}_d - \mathbf{k}_i$ during straining (Fig. 3). Its norm is related to d_{hkl} with $k = 1/d_{hkl} = 2\sin\theta/\lambda$ when the Bragg condition is satisfied. The orientation of this vector gives the direction of the strain measurement and can be described by two diffraction angles (φ , ψ) (Fig. 3). φ is the azimuthal angle, while ψ is the declination angle between the

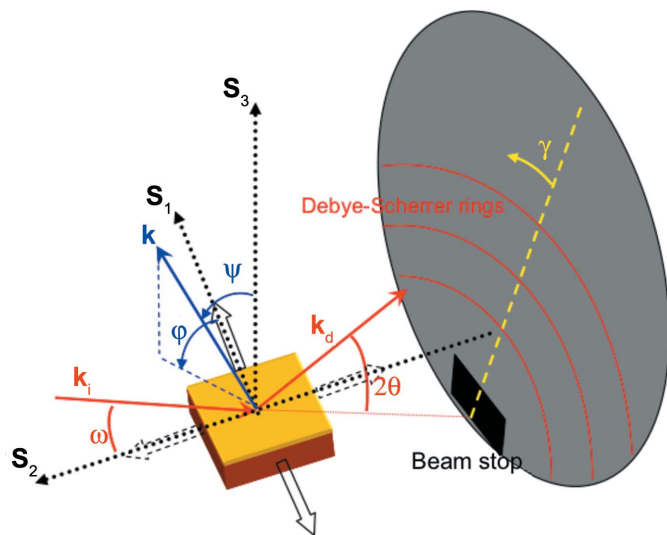


Figure 3
Sketch of the experiment showing the loaded specimen, the two-dimensional detector, the incident X-ray beam and the diffracted beam at Bragg angle 2θ . The direction of the diffraction vector $\mathbf{k} = \mathbf{k}_d - \mathbf{k}_i$ can be described by the so-called diffraction angles ψ and φ . ψ is the angle between the specimen surface normal \mathbf{S}_3 and the diffracting plane normal. φ is the rotation angle of the specimen around its surface normal (the angle between \mathbf{S}_1 and the projection of the diffraction vector \mathbf{k} in the $\mathbf{S}_1\mathbf{S}_2$ plane). γ is the angle between the vertical (dashed yellow line) and a given position on the Debye–Scherrer ring. The beamstop position is shown on the detector. ω is the incident beam angle. The wide arrows show the loading force axes.

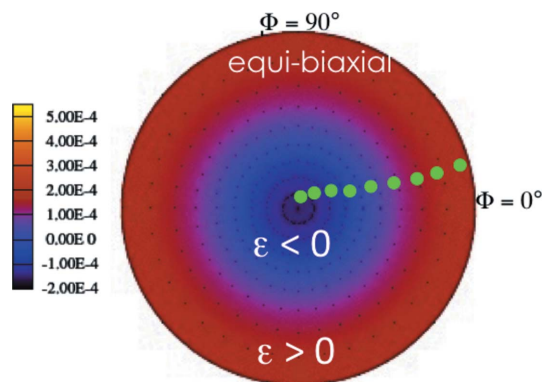


Figure 4
Calculated $\{111\}$ strain pole figure of the gold film submitted to biaxial loading with an equibiaxial stress state in the film (400 MPa) supposing that the film’s response is fully elastic. The dots show the orientations attainable in the whole γ range, namely one experimental γ path for one position of the machine.

diffraction vector and the normal to the film surface as typically used for pole-figure measurements. Both angles φ and ψ depend on

- (i) the inclination of the incident beam as referred to the sample (ω),
- (ii) the hkl reflection (θ),
- (iii) the angle γ for each Debye ring.

The relationships between the two angles φ , ψ and the angles ω , θ , γ are given by the following equations (François, 2008; Mocuta *et al.*, 2013):

$$\cos \psi = \sin \omega \sin \theta + \cos \omega \cos \theta \cos \gamma, \quad (2)$$

$$\sin \varphi = \frac{-\cos \omega \sin \theta + \sin \omega \cos \theta \cos \gamma}{|\sin \psi|}. \quad (3)$$

Fig. 4 shows a calculated SPF supposing the film response is elastic and, for one position of the machine, the attainable orientations given by φ and ψ for a full γ path on a $\{111\}$ Debye–Scherrer ring. Noticeably, the ψ range is limited at 66° by the shadowing of the loading device.

In order to measure a complete SPF, an additional azimuthal rotation (angle Φ_{sample} , see Fig. 1) is needed. Thus, a two-dimensional diffractogram was recorded every each two-degree step from $\Phi_{\text{sample}} = 0$ to 192° . We can now define the global azimuthal angle $\Phi = \Phi_{\text{sample}} + \varphi$ considering both the geometry of the setup and the rotation of the machine around its normal. In the absence of shear strain, the symmetry means that a Φ range of 180° is sufficient to describe the whole strain field.

3. Results and discussion

Fig. 5 shows the biaxial loading path (F_x as a function of F_y). Contrary to usual tests on supported thin films, a complex loading path can be followed with the DIFFABS tensile device. From the loading step labelled 2 to the loading step labelled 6, F_y was increased from 20 to 125 N keeping F_x constant ($F_x = 50$ N). Afterward, an equibiaxial stress state in

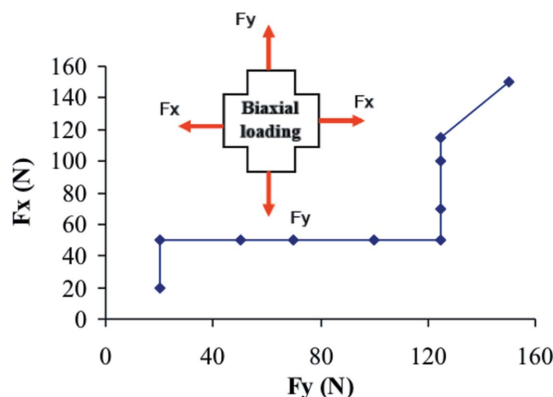


Figure 5
Loading path comprising four phases. The specimen is first loaded to the reference state (labelled 1, see Table 1). The load state is then balanced to almost uniaxial (6, Table 1), passing through an equibiaxial loading of 50 N (3, Table 1). Equibiaxial loading is then progressively recovered with the state labelled 10 (Table 1) under equibiaxial loads of 150 N.

the thin film was progressively approached by applying a load along only the x axis (from 50 to 125 N). The final point labelled 10 corresponds to an equibiaxial loading ($F_x = F_y = 150$ N). In addition, the in-plane macroscopic strains (ϵ_{xx}^{DIC} and ϵ_{yy}^{DIC}) of the substrate measured by DIC are shown in Fig. 6. Globally, when F_x (F_y) increases, ϵ_{xx}^{DIC} (ϵ_{yy}^{DIC}) increases and ϵ_{yy}^{DIC} (ϵ_{xx}^{DIC}) decreases because of the Poisson effect. It is worth noting that an equibiaxial loading ($F_x = F_y$) does not lead to equal in-plane strains (ϵ_{xx}^{DIC} and ϵ_{yy}^{DIC}), which is attributed to the in-plane mechanical anisotropy of the cruciform polyimide substrate, induced by the fabrication process. These measured strains can be used as input parameters for computing the SPFs of the supported film, assuming (i) a full transmission of the deformation at the interface and (ii) a perfect elastic behaviour of the whole film/substrate system (Fig. 4).

At each load step, a series of 96 XRD images was employed. Each two-dimensional image was corrected (beam position, tilts of the detector) and reduced to 100 one-dimensional diffractograms (2θ , intensity) using the caking function of the *FIT2D* software (Hammersley *et al.*, 1994). Au {111} and {200} peaks from each diffractogram (one for each γ and φ position, that is 9600 data points for each SPF) were fitted with a Pearson VII function and linear background in order to extract their position. The full procedure is detailed in Appendix A.

Fig. 7 presents the arrangement of experimental points placed on the SPF for $F_x = 50$ N and $F_y = 125$ N for the {200} plane family. Each line corresponds to the deformation calculated relative to the first loading step for each γ position on one image, and hence one φ position. In the subsequent figures (Figs. 8 and 9), we interpolated between the experimental points and extended by symmetry around the φ axis to obtain the overall SPF. Noticeably, in this work the ψ angle range is restricted by two geometrical constraints. Firstly, following equation (2) the value $\psi = 0$ is attainable only for the special case of $\omega = \theta$; obviously this condition can be approached for only one hkl reflection on the two-dimensional

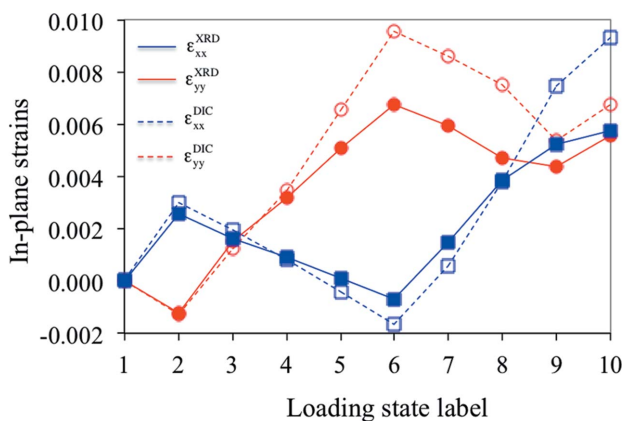


Figure 6 Principal strain evolution determined by DIC and XRD as a function of loading state label. For states labelled from 1 to 4, the strain values obtained by the two techniques superimpose, indicating the full transmission of the deformation through the interface. Instead, plasticity of the film is detected for states labelled from 5 to 10.

diffractogram. In our case, taking $2\theta_{111} \approx 20.2^\circ$, $2\theta_{200} \approx 23.2^\circ$ and $\omega = 6^\circ$, the explored range is limited at low $\psi \approx 4.1$ and 5.6° , respectively. On the other hand, the detector is shadowed by the testing machine at large $\psi \approx 60^\circ$. The latter bound depends also on ω angle with a compromise to be found in order to optimize the SPF exploration.

The measured and calculated SPFs for the two equibiaxial loadings (50 and 150 N) are shown in Fig. 8. To obtain theoretical SPFs, we incorporated the elastic constant of the gold single crystal and the actual texture of the film into a purely elastic self-consistent model (Faurie *et al.*, 2009). This model allows for taking into account the free surface effect dominant for ultra-thin films (Welzel *et al.*, 2009). On the other hand, plasticity in small and confined systems is still not fully understood (Arzt, 1998; Espinosa *et al.*, 2005; Meyers *et al.*, 2006; Van Swygenhoven & Weertman, 2006), so that it is difficult to incorporate relevant mechanical laws in such micro-mechanical models.

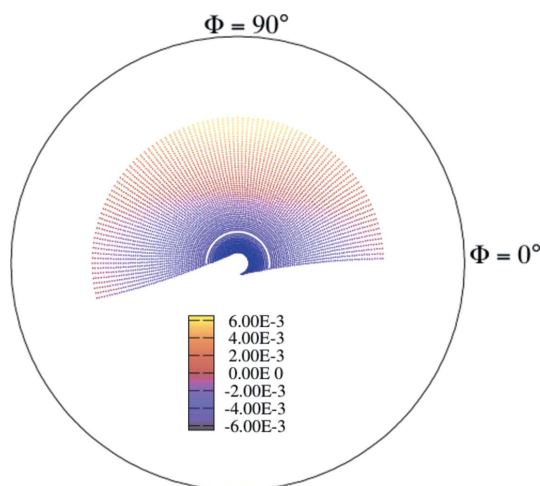


Figure 7 Experimental strain points arranged on the PF for the loading state $F_x = 50$ N and $F_y = 125$ N (loading state labelled 6, Table 1) and for the {200} plane family. Almost half of the φ angle range is obtained, while the ψ angle range is limited by both the machine shadowing and setting (ω).

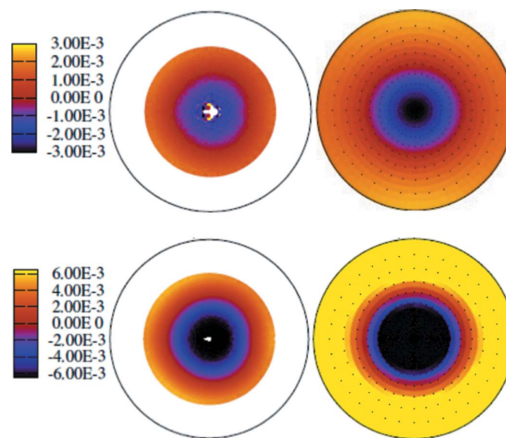


Figure 8 Experimental (left-hand side) and calculated (right-hand side) SPFs {200} under equibiaxial loadings of 50 (top) and 150 N (bottom) (loading states labelled 3 and 10, respectively; see Table 1).

In both presented cases (Fig. 8), although the applied strain field is not perfectly rotationally symmetric (Fig. 6), all SPFs show roughly a rotational symmetry. A very good agreement between experimental and calculated SPFs is obtained for the first equibiaxial load (50 N). In contrast, under 150 N equibiaxial load, the calculated SPF shows a more extended range of strain values. As discussed above, the calculation only incorporates the elastic behaviour of the film (the substrate is elastic over the entire explored range). In fact, the film response passes from elastic to elastic–plastic on loading from 50 to 150 N. This is clearly shown in Fig. 6, where we compare in-plane strains deduced from DIC and XRD analysis. In the latter case, we averaged the in-plane elastic strains estimated for the 200 and 111 reflections, following the procedure already described by Faurie *et al.* (2006). Hence the measured film XRD strains can be directly compared with applied DIC strains. In the elastic regime, the average elastic strain

Table 1

Applied biaxial loads for ten different steps.

Load ratios range from 0.4 (state 2) to 2.5 (state 6) passing through equibiaxial load (state 1, also reference; states 3 and 10).

Loading state label	Fx (N)	Fy (N)	Fy/Fx
1	20	20	1.00
2	50	20	0.40
3	50	50	1.00
4	50	70	1.40
5	50	100	2.00
6	50	125	2.50
7	70	125	1.79
8	100	125	1.25
9	115	125	1.09
10	150	150	1.00

measured by X-ray diffraction is equal to the substrate strain measured by DIC as shown by Djaziri *et al.* (2011). The XRD strains depart from DIC strains when plastic deformation or any kind of relaxation phenomenon occurs in the thin film. In the specific case of such ultra-thin films composed of very small grains in the nanometre range, a plastic size effect can be anticipated. Limited dislocation nucleation and mobility arise from grain size and boundary effects. For a metallic thin film on a substrate, deformation in the absence of any diffusive processes occurs by dislocation gliding or mechanical twinning. For very small grain size, the plastic deformation by cross slip or dislocation climb is quite restricted; dislocations may traverse the grain and are absorbed in the grain boundary. Atomic diffusion, boundary diffusion, grain boundary sliding or interface sliding can also result in relaxation. If the grain size is comparable to the film thickness, the relaxation process is dominated by grain boundary mobility (Gleiter, 2000; Espinosa *et al.*, 2005; Meyers *et al.*, 2006; Van Swygenhoven & Weertman, 2006). Microcracks can also induce strain relaxation (Graz *et al.*, 2009; Bautista *et al.*, 2010; Djaziri *et al.*, 2013). In the present experiment, this deviation appeared in between the loading states labelled Nos. 4 and 5, corresponding, respectively, to $F_x = 50$ N, $F_y = 70$ N and $F_x = 50$ N, $F_y = 100$ N (Table 1). The calculated stress components applied to the thin film for the loading state labelled No. 4 (which is still in the elastic regime) are $\sigma_{xx} = 290$ MPa and $\sigma_{yy} = 440$ MPa. It should be noted here that the complex elastoplastic loading after the elastic limit induces a rotationally symmetric X-ray strain field ($\epsilon_{xx}^{XRD} = \epsilon_{yy}^{XRD}$) for the last loading state (labelled No. 10), while this is not the case concerning the macroscopic strain field measured by DIC ($\epsilon_{xx}^{DIC} \neq \epsilon_{yy}^{DIC}$).

Fig. 9 shows that the overall SPFs change over the employed complex biaxial path starting from a reference state $F_x = 50$ N, $F_y = 20$ N (Fig. 9a). Clearly, the rotational symmetry is lost on balancing the load state to an almost uniaxial loading (Fig. 9b). This is emphasized on observing the {200} plane family for which the material is less stiff, as often encountered in metallic face-centred cubic structures (Au, Cu, Ni) (Ledbetter & Migliori, 2006). Actually, the stiffnesses of the two considered direction families ({200} and {111}) are different in a locally anisotropic material. The ratio of the X-ray elastic constants of

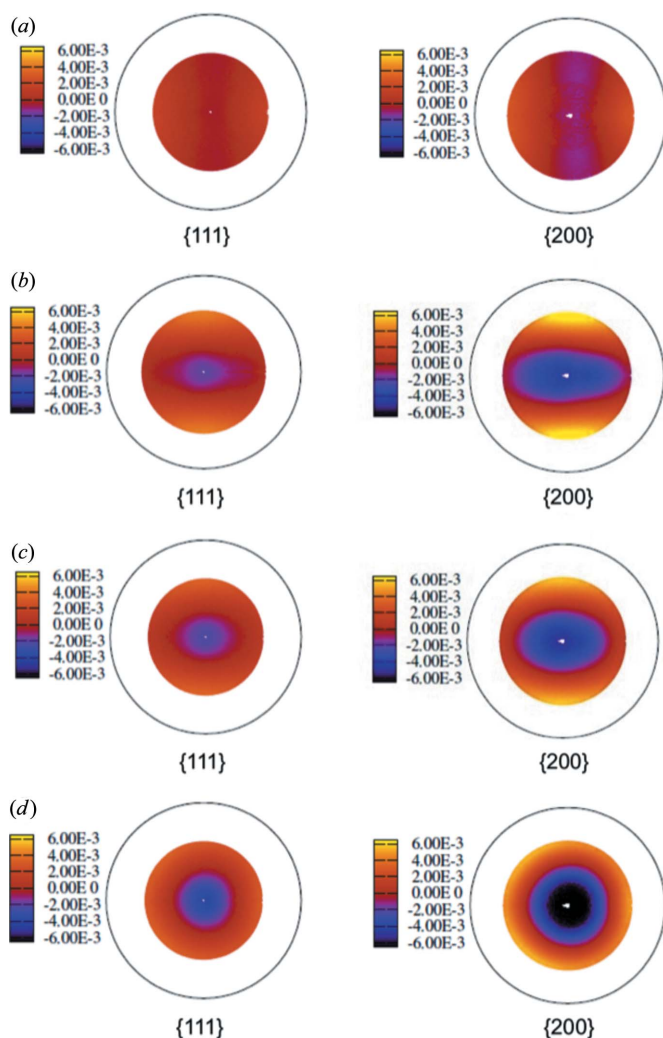


Figure 9 Experimental {111} and {200} SPFs under biaxial loading (Table 1): (a) state labelled 2 ($F_x = 50$ N, $F_y = 20$ N), (b) state labelled 6 under almost uniaxial loading ($F_x = 50$ N, $F_y = 125$ N), (c) state labelled 7 under non-equibiaxial loading ($F_x = 70$ N, $F_y = 125$ N), and (d) state labelled 10 under equibiaxial loading under 150 N.

the {200} and {111} families is about 2 (Faurie *et al.*, 2006). On recovering an equibiaxial loading (Figs. 9c and 9d), rotational asymmetry progressively vanishes for both families. Interestingly, the elastic strain PFs keep their rotational symmetry, although the in-plane macroscopic strains are different, which is attributed to the complex elastic–plastic loading path.

Noticeably, the present method for acquiring the full directional lattice strain dependence can be extended to the measurement of the orientation-dependent distribution of elastic strain heterogeneities in polycrystalline films, *i.e.* the orientation-dependent distribution of the full width at half-maximum diffraction peak. The pole figures of strain heterogeneities have been plotted for the studied ultra-thin film (not shown) and do not exhibit any significant evolution within the used loading range. However, plastic deformation at this length scale by cross slip or dislocation climb is quite restricted. This could explain the limited peak broadening for the studied ultra-thin films during elastoplastic deformation.

4. Conclusion

Ultra-thin Au supported films were biaxially stressed following a complex loading path under synchrotron X-ray diffraction. A two-dimensional detector allowed the strains for an ensemble of orientations (φ , ψ) to be scrutinized simultaneously. A complete strain pole figure was experimentally generated on rotating the loading device around its normal. The complex loading path was illustrated by a significant shape change of the strain pole figure, the strain amplitude being emphasized for the less stiff directions ($\{200\}$). For low loads, a very good agreement was found between X-ray strains in a 40 nm-thick Au film and macroscopic strains measured at the surface of the substrate, as expected in the elastic domain; the modelled strain pole figures fit very well the experimentally obtained ones. However, we found that the film deformed plastically after a loading state corresponding to $\sigma_{xx} = 290$ MPa and $\sigma_{yy} = 440$ MPa. As a result, the {111} and {200} strain pole figures were found to be rotationally symmetric for the last loading state, even though the macroscopic in-plane strains are not equal. The presented approach is appropriate for getting insight into anisotropic thin films under complex loading conditions such as those encountered in flexible devices.

APPENDIX A

Procedure to obtain SPFs

In order to obtain the pole figure from the measurements obtained at different rotations of the loading device, several steps are required.

Firstly, an important step is the calibration of the detector using certified powder (here we used NIST Cr₂O₃ powder) to correct the non-orthogonality of the detector, determine the position of the direct beam and convert pixel coordinates into (2θ , φ , ψ) coordinates.

As detailed in the main text, to determine the strain pole figure a set of two-dimensional images is acquired by rotating the machine. We used 96 images with an 8 s exposure for each strain pole figure. The rotation is carried out by moving the whole machine using the goniometer Φ_{sample} motor with a step of 2°.

For each image, we use the *FIT2D* caking function to transform the two-dimensional data into one-dimensional diagrams (2θ , intensity). Extraction of the peak position for Au {111} and Au {200} of each one-dimensional diagram is done by using a Pearson VII function embedded in an automatic procedure (Fortran and Gnuplot codes). Calculations of (φ , ψ) are made using equations (2) and (3) for each peak (so each diagram and reflection). Deformation is calculated using equation (1). This procedure is repeated for each image and for all Φ_{sample} positions.

The plot of the strain pole figure is obtained using a Gnuplot script, taking into account the (φ , ψ , ε) matrix.

References

- Arzt, E. (1998). *Acta Mater.* **46**, 5611–5626.
- Aydiner, C. C., Brown, D. W., Mara, N. A., Almer, J. & Misra, A. (2009). *Appl. Phys. Lett.* **94**, 031906.
- Bautista, J., Avilés, F., Oliva, A., Ceh, O. & Corona, J. (2010). *Mater. Charac.* **61**, 325–329.
- Bernier, J. V. & Miller, M. P. (2006). *J. Appl. Cryst.* **39**, 358–368.
- Clausen, B., Lorentzen, T., Bourke, M. A. & Daymond, M. R. (1999). *Mater. Sci. Eng. A*, **259**, 17–24.
- Dingreville, R., Qu, J. M. & Cherkaoui, M. (2005). *J. Mech. Phys. Solids*, **53**, 1827–1854.
- Djaziri, S., Faurie, D., Renault, P., Le Bourhis, E., Goudeau, P., Geandier, G. & Thiaudière, D. (2013). *Acta Mater.* **61**, 5067–5077.
- Djaziri, S., Renault, P.-O., Hild, F., Le Bourhis, E., Goudeau, P., Thiaudière, D. & Faurie, D. (2011). *J. Appl. Cryst.* **44**, 1071–1079.
- Espinosa, H. D., Berbenni, S., Panico, M. & Schwarz, K. W. (2005). *Proc. Natl Acad. Sci. USA*, **47**, 16933–16938.
- Faurie, D., Castelnau, O., Brenner, R., Renault, P.-O., Le Bourhis, E. & Goudeau, P. (2009). *J. Appl. Cryst.* **42**, 1073–1084.
- Faurie, D., Geandier, G., Renault, P., Le Bourhis, E. & Thiaudière, D. (2013). *Thin Solid Films*, **530**, 25–29.
- Faurie, D., Renault, P., Geandier, G. & Le Bourhis, E. (2011). *Thin Solid Films*, **520**, 1603–1607.
- Faurie, D., Renault, P.-O., Le Bourhis, E. & Goudeau, P. (2006). *Acta Mater.* **54**, 4053–4513.
- François, M. (2008). *J. Appl. Cryst.* **41**, 44–55.
- Fu, Q. & Wagner, T. (2007). *Surf. Sci. Rep.* **62**, 431–498.
- Geandier, G., Renault, P.-O., Teat, S., Le Bourhis, E., Lamongie, B. & Goudeau, P. (2008). *J. Appl. Cryst.* **41**, 1076–1088.
- Geandier, G., Thiaudière, D., Randriamazaoro, R. N., Chiron, R., Djaziri, S., Lamongie, B., Diot, Y., Le Bourhis, E., Renault, P. O., Goudeau, P., Bouaffad, A., Castelnau, O., Faurie, D. & Hild, F. (2010). *Rev. Sci. Instrum.* **81**, 103903.
- Gleiter, H. (2000). *Acta Mater.* **48**, 1–29.
- Graz, I. M., Cotton, D. P. J. & Lacour, S. P. (2009). *Appl. Phys. Lett.* **94**, 071902.
- Hammersley, A., Svensson, S. & Thompson, A. (1994). *Nucl. Instrum. Methods Phys. Res. Sect. A*, **346**, 312–321.
- Hild, F., Roux, S., Gras, R., Guerrero, N., Marante, M. E. & Flórez-López, J. (2009). *Opt. Lasers Eng.* **47**, 495–503.
- Keckes, J., Bartosik, M., Daniel, R., Mitterer, C., Maier, G., Ecker, W., Vila-Comamala, J., David, C., Schoeder, S. & Burghammer, M. (2012). *Scr. Mater.* **67**, 748–751.

- Kiener, D., Grosinger, W., Dehm, G. & Pippan, R. (2008). *Acta Mater.* **56**, 580–592.
- Koo, J. H., Seo, J. & Lee, T. (2012). *Thin Solid Films*, **524**, 1–19.
- Lacour, S., Jones, J., Wagner, S., Teng, L. & Suo, Z. (2005). *Proc. IEEE*, **93**, 1459–1467.
- Ledbetter, H. & Migliori, A. (2006). *J. Appl. Phys.* **100**, 063516.
- Leyland, A. & Matthews, A. (2000). *Wear*, **246**, 1–11.
- Martinschitz, K. J., Daniel, R., Mitterer, C. & Keckes, J. (2009). *J. Appl. Cryst.* **42**, 416–428.
- Mayrhofer, P. H., Mitterer, C., Hultman, L. & Clemens, H. (2006). *Prog. Mater. Sci.* **51**, 1032–1114.
- Meyers, M., Mishra, A. & Benson, D. (2006). *Prog. Mater. Sci.* **51**, 427–556.
- Miller, M. P., Bernier, J. V., Park, J. & Kazimirov, A. (2005). *Rev. Sci. Instrum.* **76**, 113903.
- Mocuta, C., Richard, M.-I., Fouet, J., Stanescu, S., Barbier, A., Guichet, C., Thomas, O., Hustache, S., Zozulya, A. V. & Thiaudière, D. (2013). *J. Appl. Cryst.* **46**, 1842–1853.
- Richard, M., Fouet, J., Guichet, C., Mocuta, C. & Thomas, O. (2013). *Thin Solid Films*, **530**, 100–104.
- Rogers, J. A., Someya, T. & Huang, Y. (2010). *Science*, **327**, 1603–1607.
- Schuren, J. C., Miller, M. P. & Kazimirov, A. (2012). *Exp. Mech.* **52**, 461–479.
- Van Swygenhoven, H. & Van Petegem, S. (2013). *Mater. Charac.* **78**, 47–59.
- Van Swygenhoven, H. & Weertman, J. R. (2006). *Mater. Today*, **9**, 24–31.
- Welzel, U., Kumar, A. & Mittemeijer, E. J. (2009). *Appl. Phys. Lett.* **95**, 111907.